

The Delta Transport Processes Laboratory: a novel laboratory for surface wave-induced currents under rotation

Paul M. Bayle^{1*}, Lennart Middelplaats², Cornel Weststeijn², Pieter van der Gaag¹, Danny de Gans², Jessamy Mol¹, Stephan van't Hof², Lars Leenheer², Jos van Meurs², Maarten Haine², Rory Mills-Williams³, Chantal A.J. Willems¹, Bas Hofland¹, and Ton S. van den Bremer¹

Abstract

Marine pollution is a major global environmental problem. The transport and dispersion of marine pollution is driven by a wide range of hydrodynamic processes, including wave-induced currents (*e.g.*, Stokes drift) that are generated by free-surface and internal gravity waves in density-stratified fluids. While the (Lagrangian-mean) Stokes drift is known to fundamentally change transport patterns, wave-induced Eulerian-mean currents, such as those generated in the presence of the Coriolis force due to the Earth's rotation, are generally less well understood. To address this, the Delta Transport Processes Laboratory (DTP-Lab), a multi-purpose lab with novel facilities and state-of-the-art equipment, is being constructed in the Hydraulic Engineering Laboratory at TU Delft. The DTP-Lab combines multiple components: a 4.40-m diameter turntable, which can support a (removable) 5-m long flume; a 12.7-m long stainless steel flume; a piston-type, wet-back, force-controlled surface wave generator; a pumping system to create any type of density stratification; and a 3D Particle Tracking Velocimetry (PTV) system. The design and construction of these components along with technical validation and performance tests are presented in this technical note. A scaling analysis demonstrates the suitability of the laboratory to investigate wave-induced current under rotation. The DTP-Lab will pioneer the combined experimental study of surface waves, density stratification and Coriolis forces. The DTP-Lab is presented here with the objective of giving practical information to future users and to describe its novelty and range of applications.

Keywords:

DTP-Lab, Turntable, Surface waves, Stokes drift, Wave-induced transport, Coriolis, PIV/PTV, Internal waves

¹ TU Delft, Faculty of Civil Engineering and GeoSciences, The Netherlands

² TU Delft, Dienst Elektronische en Mechanische Ontwikkeling (DEMO), The Netherlands

³ Edinburgh Designs Ltd, Lothian School of Technology, United Kingdom

* Corresponding author: p.b.bayle@tudelft.nl, <https://orcid.org/0000-0002-9011-7856>

Research Article. **Submitted:** 25-06-2024. **Reviewed:** 16-06-2025. **Accepted** after double-blind review: 02-08-2025. **Published:** 27-08-2025.

DOI: [10.59490/jchs.2025.0047](https://doi.org/10.59490/jchs.2025.0047)

Cite as: Bayle, P.M., Middelplaats, L., Weststeijn, C., Van der Gaag, P., De Gans, D., Mol, J., Van 't Hof, S., Leenheer, L., Van Meurs, J., Haine, M., Mills-Williams, R., Willems, C.A.J., Hofland, B., Van den Bremer, T.S., The Delta Transport Processes Laboratory: a novel laboratory for surface wave-induced currents under rotation, Journal of Coastal and Hydraulic Structures, 47, DOI: 10.59490/jchs.2025.0047

This paper is part of the **Thematic Series** of selected papers on advances in physical modelling and measurement of Coastal Engineering issues, as presented on the Coastlab Conference in Delft in 2024.



The Journal of Coastal and Hydraulic Structures is a community-based, free, and open access journal for the dissemination of high-quality knowledge on the engineering science of coastal and hydraulic structures. This paper has been written and reviewed with care. However, the authors and the journal do not accept any liability which might arise from use of its contents. Copyright © 2025 by the authors. This journal paper is published under a CC BY 4.0 license, which allows anyone to redistribute, mix and adapt, as long as credit is given to the authors.



1 Introduction

The presence of marine pollutants, such as marine plastics, has increased significantly over the last decades and poses a major environmental problem (Moulton et al., 2022; Sutherland et al., 2023). Marine pollutants are transported, mixed, and diffused in the ocean, which means understanding and modelling marine transport is key for mitigation purposes (van Sebille et al., 2020; Moulton et al., 2022). However, the physical mechanisms involved in marine transport in both nearshore and offshore ocean environments are not yet fully understood.

Marine transport is driven by a wide range of processes, from large-scale geostrophic currents to small-scale turbulent mixing in the upper-ocean boundary layer (van Sebille et al., 2020; Sutherland et al., 2023), and wave-induced transport is an important example. The most well-known form of wave-induced transport is the Stokes drift (Stokes, 1847; van den Bremer and Breivik, 2017). The Stokes drift arises from the periodic motion that a particle experiences under the action of a wave – under a wave crest, a particle moves forwards further than it moves backwards under the trough – and therefore occurs for surface waves (Grue and Kolaas, 2017; Paprota et al., 2016; van den Bremer et al., 2019b; Calvert et al., 2019), but can also occur for certain types of internal gravity waves propagating in density stratified fluids (van den Bremer et al., 2019a; Weber et al., 2023). Stokes drift is essentially the difference between a Lagrangian-mean and a Eulerian-mean velocity; it transports tracers in the direction of the waves and can fundamentally change transport patterns in the ocean (Iwasaki et al., 2017; Fraser et al., 2018; Dobler et al., 2019; Onink et al., 2019).

Previous numerical simulations of marine transport have simply superimposed the Stokes drift onto the Eulerian-mean current field obtained from large-scale circulation models, without taking into account the fact that the Eulerian-mean flow is itself modified by waves. The total (Lagrangian-mean) wave-induced velocity relevant for pollutant transport is the sum of the Stokes drift and the wave-induced Eulerian-mean current. For surface waves, this wave-induced Eulerian-mean current can arise due to the presence of wave groups (Longuet-Higgins and Stewart, 1962; van den Bremer et al., 2019b; Calvert et al., 2019), in (viscous) wave-driven boundary layers such as at the bed, due to the interaction between waves and turbulence (Pearson, 2018), and when waves shoal near coasts in the form of a cross-shore undertow and longshore currents (see Hansen and Svendsen, 1984; Hwung and Lin, 1991; Matsunaga et al., 1994; Lentz and Fewings, 2012; Pezerat et al., 2022, among many others). It also arises due to the rotation of the Earth through the Coriolis–Stokes force (Ursell, 1950; Hasselmann, 1970; Higgins et al., 2020; Cunningham et al., 2022). For internal waves, wave-induced Eulerian-mean flows are less well understood but also arise due to the presence of wave groups (van den Bremer et al., 2019a). Beyond the fact that some of these processes have not been studied in physical laboratory experiments (*i.e.*, wave-induced currents associated with surface waves under rotation and internal waves), the theoretical and numerical frameworks used to study them rely on simplifications and assumptions that still need to be tested and validated using physical modelling. In addition, the laboratory requirements for such physical modelling to be performed and the three-dimensionality of the problems lead to technical challenges that explain the lack of existing laboratories suitable for the investigation of these processes.

With the motivation to better understand marine transport in the nearshore environment, the Delta Transport Processes Laboratory (DTP-Lab) was developed at TU Delft, as a novel and dedicated section of the existing Hydraulic Engineering Laboratory. The DTP-Lab aims to pioneer the combined experimental study of surface waves, internal gravity waves in density stratified fluids, and Coriolis forces in a single laboratory. The DTP-Lab is designed to be user-friendly, with a multi-purpose vision enabled by an interchangeable wavemaker and state-of-the-art measurement equipment. To inform future users, this technical note presents the DTP-Lab facilities (some parts are still under construction) and equipment that make this laboratory unique.

The remainder of this technical note is structured as follows. Section 2 describes the design, construction and capabilities of each component of the DTP-Lab. Section 3 presents the technical performance of the key components designed by those who contributed to the development of the DTP-Lab (the authors of this technical note). Section 4 explores which part of the relevant parameter space can be studied in the DTP-Lab by considering relevant dimensionless numbers for waves under rotation, as well as the novelty of the DTP-Lab compared to other existing facilities. The main conclusions are outlined in Section 5.

2 The DTP-Lab development

The Delta Transport Processes Laboratory (DTP-Lab) is developed as part of the existing Hydraulic Engineering Laboratory at TU Delft. The DTP-Lab facilities and equipment are complementary to each other. In this section, each component is presented, discussing the motivation of its design, construction (when applicable), and its capabilities. A detailed description of the design and construction is given for the turntable (Section 2.1) and the density stratification

pumping system (Section 2.5), since these components were designed and constructed by the authors, while the others were purchased from external suppliers.

2.1 The turntable

To reproduce the Coriolis force at laboratory scale, a rotating system is required. Existing large-scale (the Coriolis platform, 13 m in diameter, LEGI, Grenoble, France, see Mercier et al. (2012)) and medium-scale (the TurLab rotating tank, 5 m in diameter, University of Turin, Italy, see Suino et al. (2017); the Coriolis rotating tank, 5 m in diameter, the University of Science and Technology in Trondheim, Norway) rotating basins have demonstrated the research relevance of such facilities. However, rotating basins provide constraints, whereas vertically flat turntables (*e.g.*, the 1.67 m turntable at Eindhoven University of Technology, the Netherlands) are more versatile. It was therefore decided to design a medium-scale, flat turntable of 4.40 m in diameter.

The turntable is composed of a base frame of 2.1 m in diameter, on which a 1.93-m diameter bearing ('wire race bearing' from Franke) is fixed (Figure 1a and b). A frequency-controlled motor (from SEW-EURODRIVE, 4 kW, in blue in Figure 1c) is placed on the base frame and drives the rotation through a gear head in contact with the bearing teeth (Figure 1d). Using adjustable levelling feet, the base frame and the bearing are levelled down to a 10th of a millimeter, to ensure a near perfectly vertical axis of rotation.

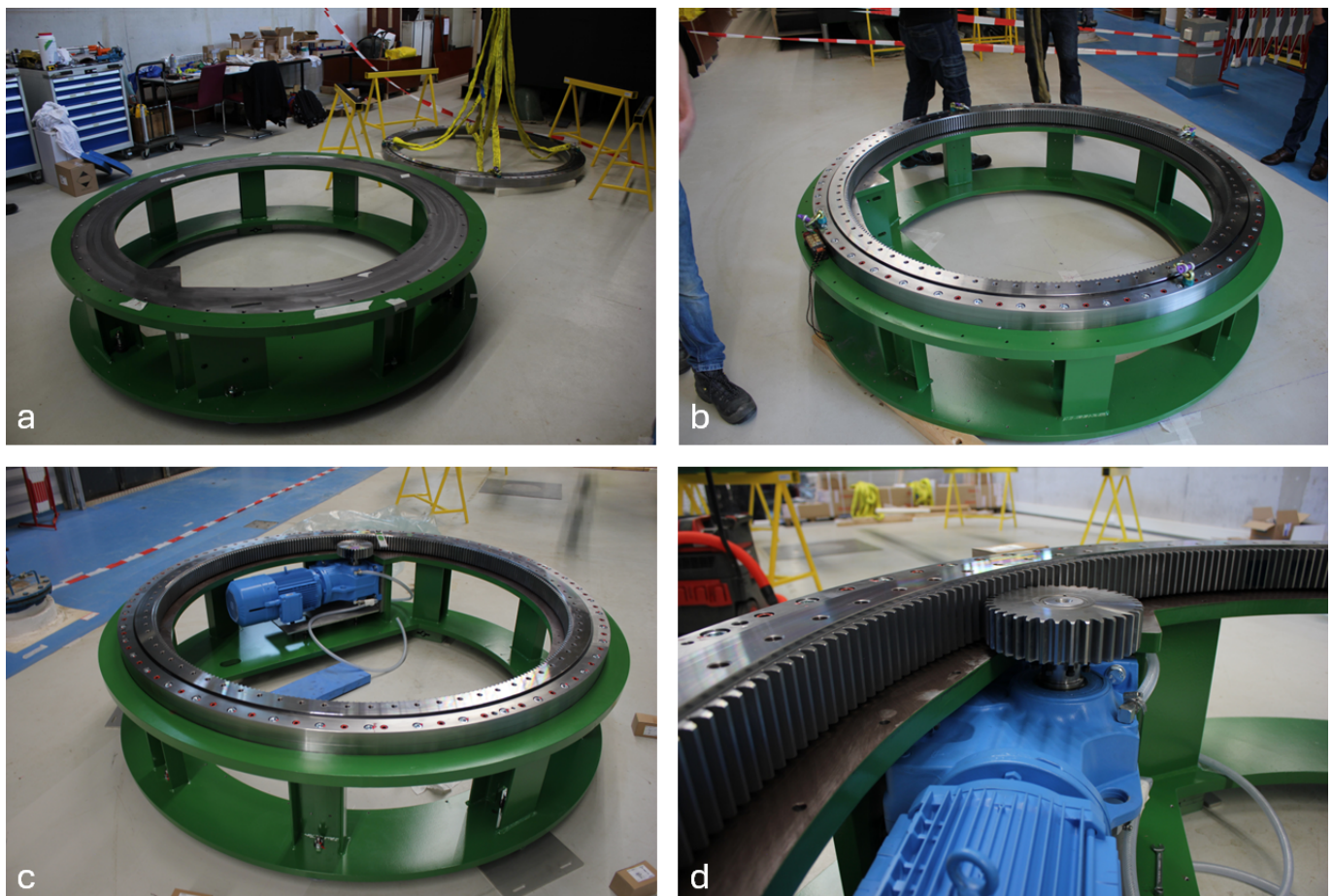


Figure 1: Photographs of: a) the bare base frame (*at the front*) next to the bearing (*at the back*); b) the assembled bearing and base frame, c) including the motor; and d) the motor gear head aligned with the bearing.

The rotating part of the table, the top frame, consists of four custom-made manufactured segments assembled on site (Figure 2a,b). The top frame is then bolted to the rotating part of the bearing (Figure 2c). The table deck is constructed using 20 mm thick custom-made aluminium plates separated by flexible rubber seals to ensure water tightness. Some segments are removable for maintenance purposes, and four hatches (black squares in Figure 2d) allow instruments' cables to run from the table to the PC storage cabinets located underneath the table. Each cabinet can accommodate 100 kg of equipment and has a storage area of 190 dm² (visible in Figure 3a). The table deck has multiple M8 threaded holes spaced over the surface to allow instrument fixation (Figure 2d). A removable and

adjustable overhead frame (for instrumentation) is installed on top of the table (Figure 3). It consists of four poles holding an adjustable horizontal frame that can reach a maximum height of 3.30 m above the table.

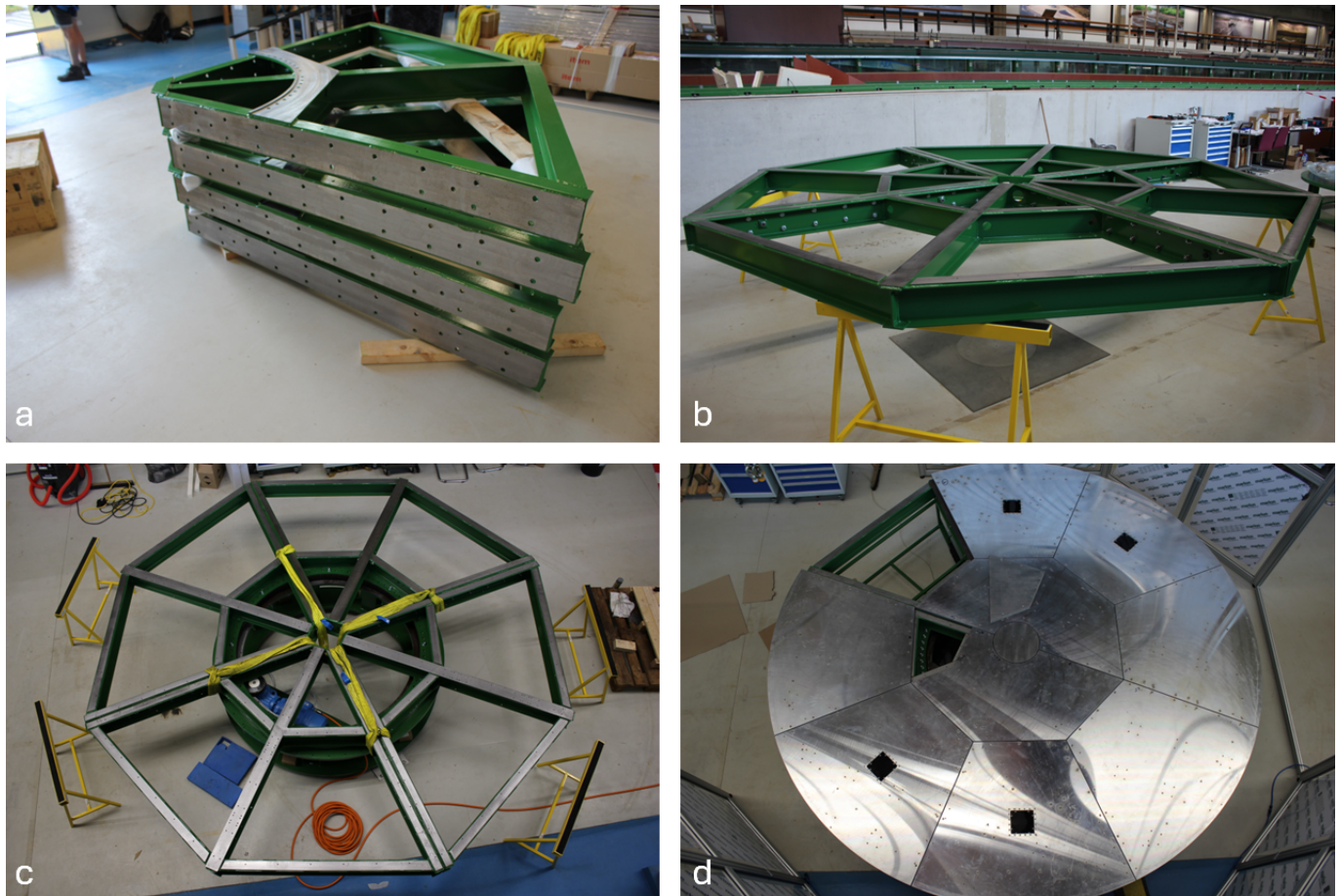


Figure 2: Photographs of: a) the four custom-made segments of the turntable's top frame; b) the assembled segments of the top frame; c) the assembled bottom and top frame; d) the aluminium table deck. The hatches and M8 threaded-hole pattern are visible.

For safety reasons, the table is enclosed by a fence (Figure 3), ensuring rotation can only occur when all doors are locked. Safety stop buttons are placed at a few locations inside and outside the fence, trigger a safe emergency stop (at fixed deceleration, so no sudden stop) and cut the power on the table.

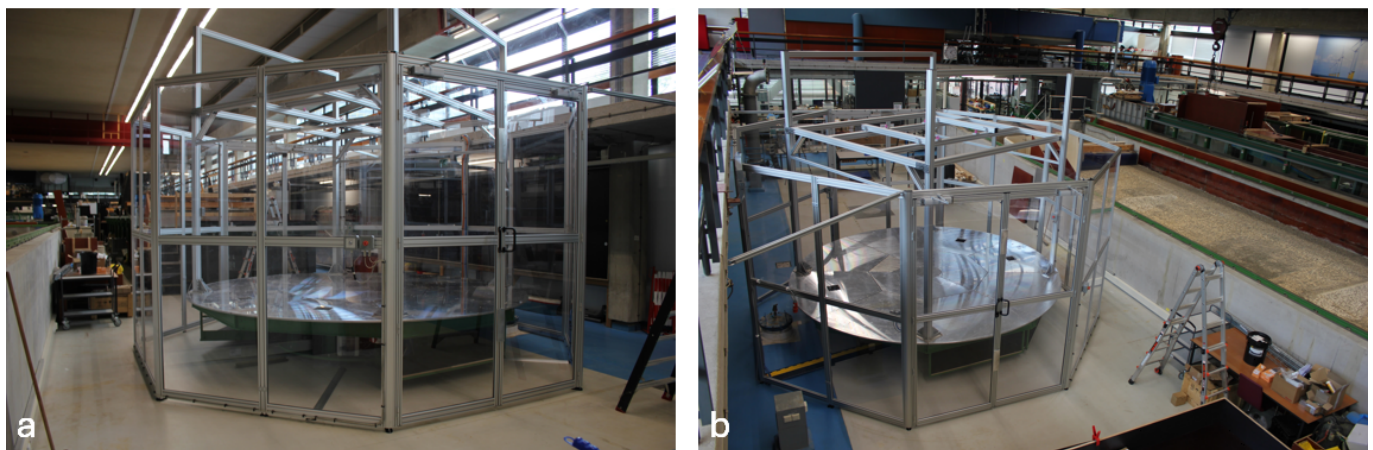
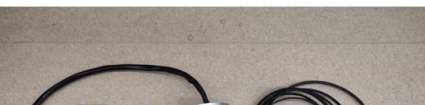


Figure 3: Photographs of the completed construction, including the turntable, overhead frame and the safety fence: a) viewed from the lab floor, b) viewed from the upper floor balcony.

Power is brought to the table through a custom-made slip-ring from Gileon (Figure 4). The slip-ring delivers power in the form of three-phase at 16 Amp and three single-phases at 16 Amp, as well as an Ethernet connection to the table. Power sockets are located next to each storage cabinets underneath the table.



Technical specification						
Group	Power 1	Power 2	Signal	1000Mbps		
Circuits	1~5	6~14	15~24	25~36		
Rated voltage/current	400V/16A	230V/16A	24V/5A	--V/--A		
Dielectric strength	500VAC@50Hz.60s		200VAC@50Hz.60s			
Insulation resistance	≥500MΩ/500VDC		≥200MΩ/200VDC			
Dynamic contact resistance	≤10mΩ					
Contact material	Precious metals					
Frame material	Aluminum					
Operating Speed	0~250rpm					
Operating Temperature	-20℃~+80℃					
Sealing degree	IP54					

Figure 4: a) Photographs and b) technical specifications of the custom-made slip-ring.

The complete table and overhead frame weigh 5 tonnes and can accommodate a further 10 tonnes. The rotation speed ranges from 0.01 to 7.50 rotations per minute (rpm), at increments of 0.01 rpm (± 0.002 rpm). The table is controlled via a simple digital user interface, from which the user can decide on the rotation speed and direction (positive clockwise and negative anti-clockwise). The acceleration and deceleration to the desired speed is fixed to 0.248 rpm/s and embedded within the control system (including the safety-stop procedure), but can be changed if necessary. Instruments on the table can be remotely controlled via Ethernet or WiFi connection, and a working platform next to the table is available for users.

2.2 The rotating flume

To study the effect of the Coriolis force on the wave-induced current generated by free surface waves, a flume that can be placed on the turntable was designed and built by Edinburgh Designs Ltd. The flume is 5 m long, 0.5 m wide and 0.5 m deep; it is placed on a support frame, giving a total height of 1.40 m. The bottom and sidewalls of the flume are made of low-iron toughened PVB laminated glass (providing full optical access), except for the section that accommodate the surface wave generator which is made of stainless steel 316 (Figure 5a). The flume is mounted on a support beams (large green beams at the bottom of the flume, see Figure 5a) that reinforces the whole flume during hoisting and rotation. The flume can be levelled to sub-millimetre precision with levelling feet placed at the bottom of the support beams. The rotating flume can be lifted on and off the table, and levelled in place (Figure 5a and b).

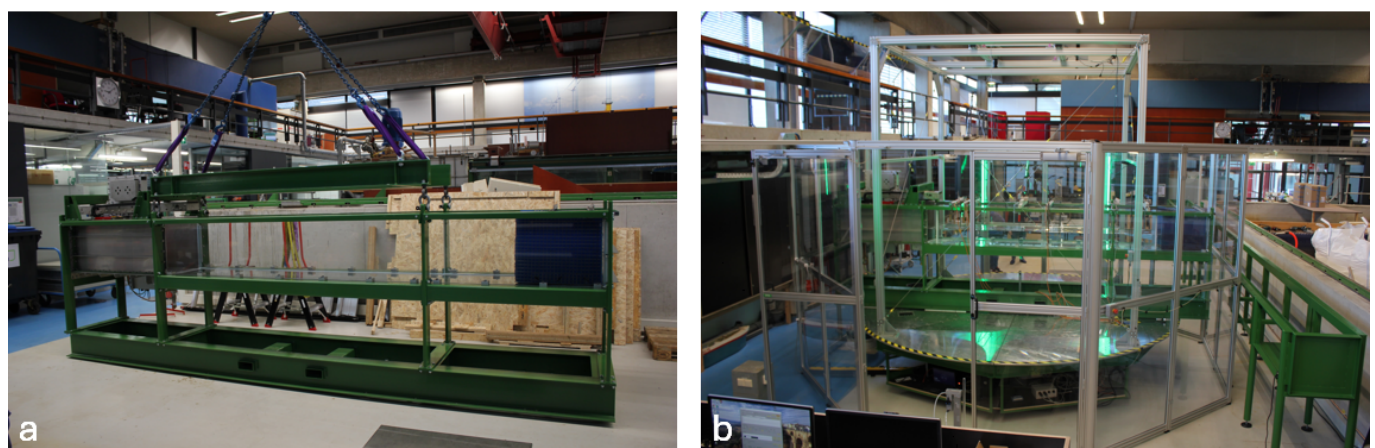


Figure 5: Photographs of a) the rotating flume, equipped with the surface wavemaker (left) and foam absorber (right), during hoisting. A lifting frame is attached to the flume for this purpose. b) the complete set-up with the rotating flume on the turntable, with the control platform in the foreground and the internal wave flume on the right hand side.

The flume has one inflow/outflow compartment (stainless steel 316) at the bottom and across the whole width of the flume, facilitating the filling and draining. This compartment can easily be equipped with a filter system to collect

any particles (*e.g.*, fluorescent particles used with the 3D PTV system, see Section 2.7). There is no corrodible metal in direct contact with water, allowing the flume to be filled with salt water, although it is recommended to limit the number of experiments using salt in this flume.

The flume is equipped with a custom made mesh/foam wave absorption system (the blue part on the right-hand side in the flume in Figure 5a), of either 60 cm or 85 cm in length (two fixed length possible). This system damps between 85 and 95% of the wave energy, depending on the wave frequency. This level of absorption is common in flume experiments, and as a result, the wave field always contains a reflected wave component. This is realistic for nearshore experiments but not necessarily for those in deep water. As with all laboratory flumes, the presence of reflections must be taken into account by users and may be prevented further by optimising beach design. Note that planar slopes (purpose built from wood or Plexiglas) can also be used. These wave absorption systems can also be placed inside the stainless-steel salt-water flume (see Section 2.3).

2.3 The salt-water flume

With the primary objective of (but not limited to) studying internal gravity waves propagating in a density stratified fluid (salt water), a stainless steel flume 12.7 m long, 0.5 m wide and 0.5 m deep was designed and constructed by Van der Velde Delft B.V. (Figure 6). The flume is placed on a support frame, giving a total height of 1.40 m. The flume is entirely made of stainless steel 316 and glass, and is permanently installed in the laboratory. The end section, on the right-hand side of Figure 6, is made of stainless steel and can accommodate the surface wave generator (see Section 2.4). The left-hand side end, over a distance of 600 mm, is designed to accommodate an internal gravity wave generator (Section 2.6). The bottom of this latter section is made of stainless steel, and the end wall consists of a removable watertight stainless steel plate. The bottom and sidewalls of the flume are made from toughened laminated glass, providing full optical access.

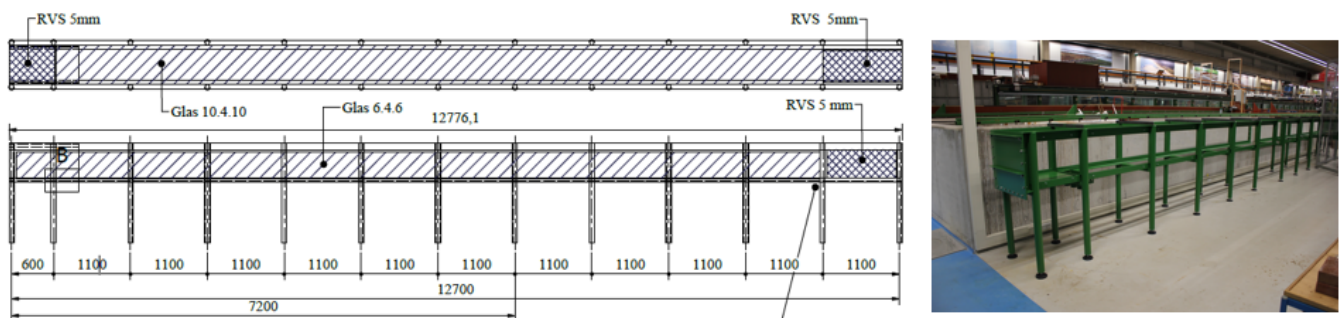


Figure 6: (Left: Top (top panel) and side view (bottom panel) of the stainless steel flume. Dimensions are given in millimetres. Design drawing by Van der Velde Delft B.V. Right: photograph of the stainless steel salt-water flume.

The salt-water flume has two inflow/outflow compartments, similar to the one presented in Section 2.2. Two vertical gates (one at 0.6 m and one at 7.2 m measures from the left end of the flume, see Figure 6) can be slid into vertical slots made in the sidewalls to create a watertight separation. This is designed to shorten the flume if needed, but also to perform lock-release experiments (*e.g.*, dam break, tsunamis) with or without salt-water. The system is manual, but allows for automation at a later stage.

Removable lids, which consist of a series of 1.1-m-long aluminium frames on which Plexiglas plates are attached through threaded rods, can be fixed on top of the flume sidewalls. The Plexiglas plates can then be lowered down to the free surface in order to prevent surface waves from developing when internal waves are generated. This lid system can also be used in the rotating flume, since both flumes have the same width.

2.4 Surface wave generator

A force-controlled piston, wet-back surface gravity wave generator was designed by Edinburgh Design Ltd. (Figure 7a). It is powered through a self-contained cabinet and can be used in both flumes. The wavemaker has a total stroke of 0.5 m, and the gap between the paddle and the sidewalls is kept below 0.3 mm over the whole stroke. The zero-position of the paddle is 0.80 m from the back end of the flume. In collaboration with Edinburgh Design Ltd., the wave generation software is being enhanced and upgraded for this specific project.

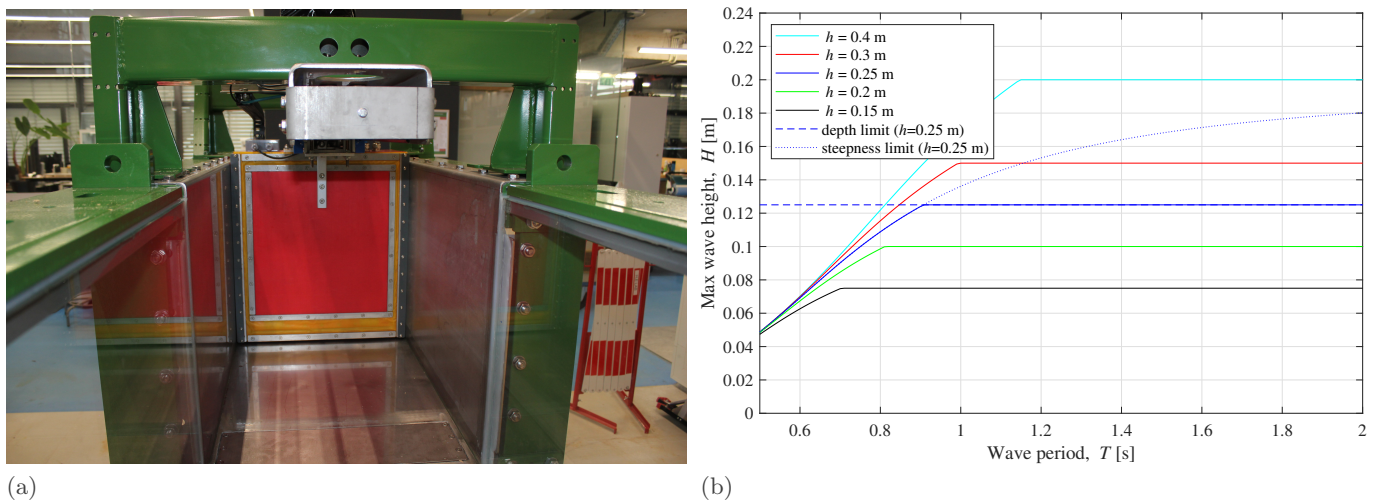


Figure 7: a) Photograph of the surface gravity wave generator in the rotating flume, b) Surface gravity wave generator specification for regular waves: wave height as a function of wave period for different water depths h . The depth limit (dashed line) and steepness limit (dotted line) used to make this plot are displayed for a water depth of $h = 0.25$ as an example.

The surface wave generator can operate in 0.15–0.40 m water depth, and generate waves of $H_s = 0.05$ –0.20 m and $T_p = 0.5$ –2 s. The specifications for regular waves are given in Figure 7b, where for a given water-depth curve, any combination of wave period and wave height below that curve is feasible. The steepness limit (dashed line) used is $H_b/L_b = 0.125 \tanh(kh)$ from Miche (1944), and the depth limit (dotted line) used is the expression for a flat bottom, $H_b/h_b = 0.5$ from Chen et al. (2022) (the subscript ‘b’ indicates ‘at breaking’). These limits are displayed for $h = 0.25$ m as an example. The stroke was designed to be large enough to generate and absorb long sub-harmonics waves.

2.5 Pumping system for density stratification

Layers (or a continuum) of fluid of different densities naturally form in ocean, and waves known as internal gravity waves can propagate on this stratification within the fluid. To study internal gravity waves in the laboratory, it is essential to be able to create a density stratification in a flume – *i.e.*, variation of the fluid density with the vertical. This can be achieved by using different types of fluids (*e.g.*, water and Isopar V, Weber et al., 2023)) or more commonly by using salt water with different salt concentrations (*e.g.*, Allshouse and Swinney, 2020). There are different types of stratification that one may want to create, depending on the type of internal waves and processes to study. The most simple one is a ‘two-layer’ stratification, which consists of a lighter layer of fluid on top of a layer of denser fluid. This allows the investigation of ‘interfacial waves’, propagating at the interface between the two fluids. The thickness of the interface can also be increased, with the density varying linearly from the denser bottom fluid to the less dense top fluid. This ‘top-hat’ stratification mimics the thermocline of a natural ocean system. Finally, stratification with a continuous change of density over the whole water column, such as a linear or an exponential profile may be chosen. To generate all these types of stratification, it is crucial to have a pumping system that allows a precise and accurate construction of the density profile.

Based on the literature and what is used in other internal wave facilities (Horn et al., 2001; Allshouse and Swinney, 2020), the authors designed and developed a complete pumping system. The system differs from the common double-bucket method (Hill, 2002), because firstly, the double-bucket method is not suitable for complex density profiles and secondly, modern technologies allow for a more space-effective system. The pumping system designed is sketched in Figure 8. It consists of a large reservoir of 800 L, in which salt-water (brine) is prepared at a high concentration (200–250 parts per thousand) by mixing fresh water and salt. A second, small reservoir of 50 L is continuously filled with fresh water up to a specified level. The densities and temperatures of both fluids are measured prior the creation of a stratification, using an Handheld Density Meter, DMA 35 from Anton Paar. The rest of the system consists of two pumps: pump F pumps water from the fresh-water reservoir, and pump S pumps water from the salt-water reservoir (Figure 8). The two flows are mixed together by a static mixer (*i.e.*, a pipe with fixed blades through which the liquids flow), to obtain a homogeneous mixture at the outlet of the mixer. The mixture then slowly flows into the laboratory flume through the inflow compartment. The (stable) stratification is therefore created starting from the lowest to the highest density of the desired profile.

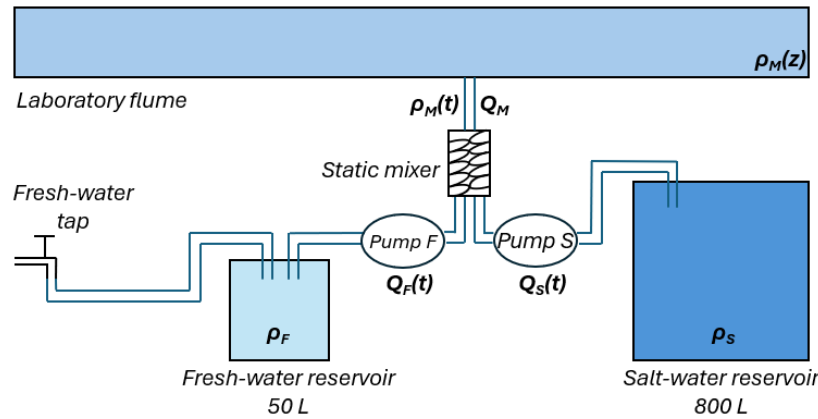


Figure 8: Conceptual sketch of the pumping system used in the DTP-Lab.

The flow rate at which the water is pumped from each reservoir is a function of the desired density profile, and is determined solving the equations for conservation of volume and mass:

$$Q_M(t) = Q_S(t) + Q_F(t), \quad (1)$$

$$Q_M(t)\rho_M(t) = Q_S(t)\rho_S + Q_F(t)\rho_F, \quad (2)$$

with $Q_F(t)$, $Q_S(t)$ and $Q_M(t)$ the fresh-water, salt-water and mixture (entering the flume) flow rates, respectively; and ρ_F , ρ_S and $\rho_M(t)$ the fresh-water, salt-water and mixture densities, respectively.

The densities ρ_F , ρ_S are constant and known. The flow rate $Q_M(t)$ is also set to be constant, and is a function of the time allowed to fill up the flume as well as the maximum acceptable flow rate to fill the flume without creating too much turbulence. The vertical density profile $\rho_M(z)$ is known, and needs to be converted into $\rho_M(t)$. To achieve this in practise, the filled flume is discretised into thin sub-layers, each of known concentration and volume. Starting from the top of the profile and working downwards, the relation between z and t (*i.e.*, $\rho_M(z)$ and $\rho_M(t)$) is determined by calculating how much time it takes for each of these sub-layers to flow into the laboratory tank, thus taking into account any known bathymetry variations in the flume. Finally, Eq. 1 and Eq. 2 are solved for $Q_F(t)$ and $Q_S(t)$.

Two computer-controlled peristaltic pumps are used (MSE Pro, model LS0331 with pump head YZ35-13), and can pump at a flow rate between 1.3 to 12000 mL/min. The lower limit allows enough density discretisation between sub-layers, while the higher limit is large enough to fill up the flume in less than 4 hours. The system is fully automated and controlled using a user interface. The water is recycled as much as possible via the salt-water reservoir, and the remaining water is diluted down to a suitable density before being disposed through the sewer. Note that the pumping system is to be used primarily with the stainless steel flume, but density profiles can also be created in the rotating flume if necessary.

2.6 Internal gravity wave generator

A novel prototype of internal wave generator, based on the concept developed by Gostiaux et al. (2007), is proposed for future DTP-Lab development, but has not been constructed (Figure 9). The generator would consist of a series of horizontal plates stacked vertically in a drawer-type of structure, which would allow each plate to move back and forth horizontally. Based on the existing prototype at ENS Lyon (Dossmann et al., 2017), each plate would be connected to a stepper motor (one motor per plate) via a rod (coloured green in Figure 9a), and each motor would be controlled independently. The plates would therefore be fully independent from each other. As a result, the vertical shape formed by the plates will allow control of the velocity-depth structure in space (vertically) and in time over an experiment. This system would have the capability to generate 1) irregular waves time series (from a range of spectrum) during a single experiment, and 2) isolated wave groups, both with the complete velocity-depth structure. The stepper motors will allow for a horizontal motion with maximum amplitude of ± 20 mm. Each plate will be 8 mm thick, with a 0.7 mm gap between the plates.

A simple interface will allow the user to specify the time series of position for each plate required to generate the variation over time of the complete vertical shape. While the motors located outside of the water will be relatively well ventilated, it is expected that using the system continuously for more than two hours will lead to local heating, hence disturbance and modification of the density stratification near the generator. It is therefore recommended to keep the duration of experiments run shorter than two hours.

Note that this wave generator could also be placed in the rotating flume, since a density stratification can also be created in this flume. Therefore, Coriolis effects could be combined with internal waves in the shorter rotating flume if necessary.

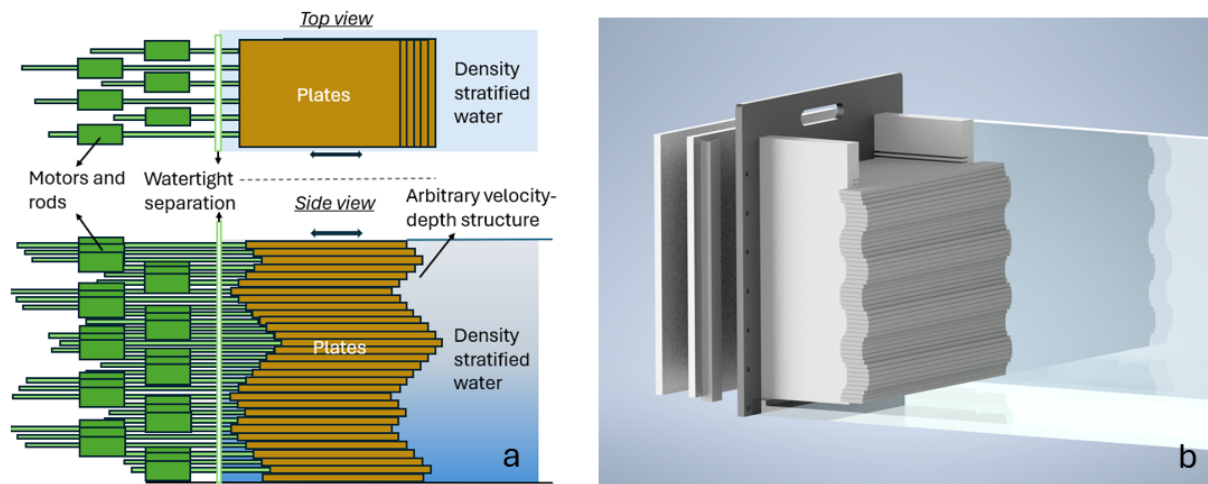


Figure 9: a) Conceptual design drawing of the internal wave generator, b) Design drawing of the prototype in the flume.

2.7 PTV system

In addition to standard laboratory instrumentation (*e.g.*, wave gauges, cameras and ADVs available in the Hydraulic Engineering Laboratory at TU Delft), the DTP-Lab has a dedicated 3-dimensional Particle Tracking Velocimetry (3D PTV) system. The system, a 'MiniShaker' from LaVision (Figure 10), consists of four cameras affixed onto a box with set positions and angles. The system is used with LED light (2 LED boxes of 300 by 100 mm, see Figure 10). The boxes are generally placed underneath the flume, to illuminate a volume of water, while the Minishaker is placed by the side of the flume. Using neutrally-buoyant micro-particles as tracers (diameter ranges from 20-150 μm), images of illuminated particles are recorded (at a frequency of up to 100 Hz). Fluorescent particles can also be used to limit the effect of light reflection from the free surface and flume glass.

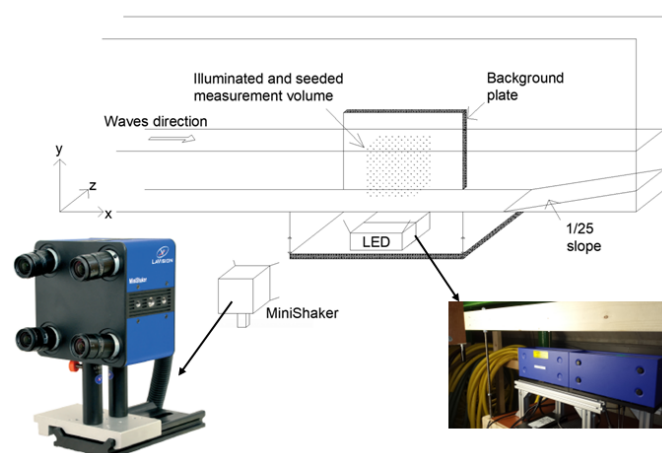


Figure 10: Sketch of the set-up used to test the 3D PTV system in a wave flume (39 m long, 0.79 m wide and 1 m high, not part of the DTP-Lab), measuring the wave-induced current. Photographs of the MiniShaker and LED boxes are also displayed.

The system was purchased with the state-of-the-art 'Shake-the-box' data processing software for particle tracking (Schanz et al., 2016). This software allows the tracking of particles in space and time within the volume of water. Lagrangian velocities are obtained from the trajectories, and Eulerian velocities can be reconstructed (Sciacchitano

et al., 2021; Sellappan et al., 2020), leading to a complete high-resolution 3D analysis of the flow. The LaVision MiniShaker is a relatively user-friendly system that allows inexperienced users to easily set-up and calibrate the system, and obtain a large 3D PTV dataset.

3 Technical results: system performance

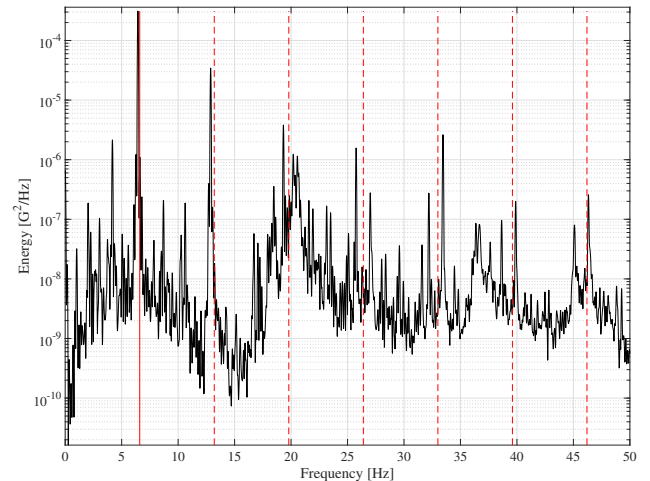
3.1 Turntable alignment and vibration

One of the key objectives in the design and construction of the turntable is to have a nearly perfectly vertical axis of rotation. The assessment of the verticality consists of measuring the elevation of a fixed point on the table (above the bearing, at 0.96 m from the centre) for six different table angular positions, using an optical level with an accuracy of a tenth of a millimetre. A total vertical deviation of 0.1 mm was measured above the bearing. This corresponds to a deviation of 0.003 degrees of the axis of rotation from the vertical, which is assumed negligible.

The second key objective is to limit the amount of vibration on the table and overhead frame, and quantify these for all rotation speeds. Vibrations were measured with two sets of three accelerometers (Q-FLEXQA-750, recording at 500 Hz), installed in three directions on the outer part of the table frame (Figure 11a), and near the centre of the overhead frame. The variance density spectrum of the detrended acceleration time series was obtained with a fast Fourier transform, using Hamming-window of 40 seconds with 50% overlap. A typical spectrum is shown in Figure 11b. Note that the acceleration is divided by 9.81 m/s^2 , hence given in G . The main peak (plain red line in Figure 11b) is associated with the frequency of the teeth of the bearing-gear head assembly, which can be calculated using the rotation speed and the number of teeth (the bearing has 330 teeth and the gear head 60), while the other peaks (dashed red lines) corresponds to its harmonics. A wide peak around 19.3 Hz is visible for all rotation speeds and seems to be the resonance frequency of the whole table.



(a)



(b)

Figure 11: a) Photograph of the three accelerometers, measuring in the x (tangential), y (radial) and z (vertical) directions; b) Example of a variance density spectrum of the acceleration in the x -direction, for a rotation speed of +1.2 rpm. The continuous red line marks the teeth frequency of the bearing-gear head assembly, and the dashed red line its harmonics (1st to 6th).

The root mean square ($G_{rms} = \sqrt{\eta_{acc}^2}$ where η_{acc} is the detrended acceleration time series and the overbar is the mean) and the spectral second-order moment period (T_{m02}) of the vibrations were calculated. Figure 12 shows these bulk parameters as a function of the rotation speed, for both the table and overhead frame.

G_{rms} is very small in all directions, on both the table and overhead frame. It significantly increases for rotation speeds around ± 3.5 rpm, which corresponds to the frequency of the teeth of 19.25 Hz, hence amplifying the resonance frequency of the table of 19.3 Hz (Figure 11b). Generally, positive rotations generates more vibrations than negative rotations. T_{m02} is kept below 0.2 s on the table and 0.1 s on the overhead frame. The period follows the trend of the bearing-gear head assembly curve (Figure 12), but is generally below for small and medium rotation speeds. To limit interference with experimental set-up, we therefore recommend avoiding rotation speed between ± 3.3 -3.7 rpm, and

prioritise negative rotation (*anti-clockwise*).

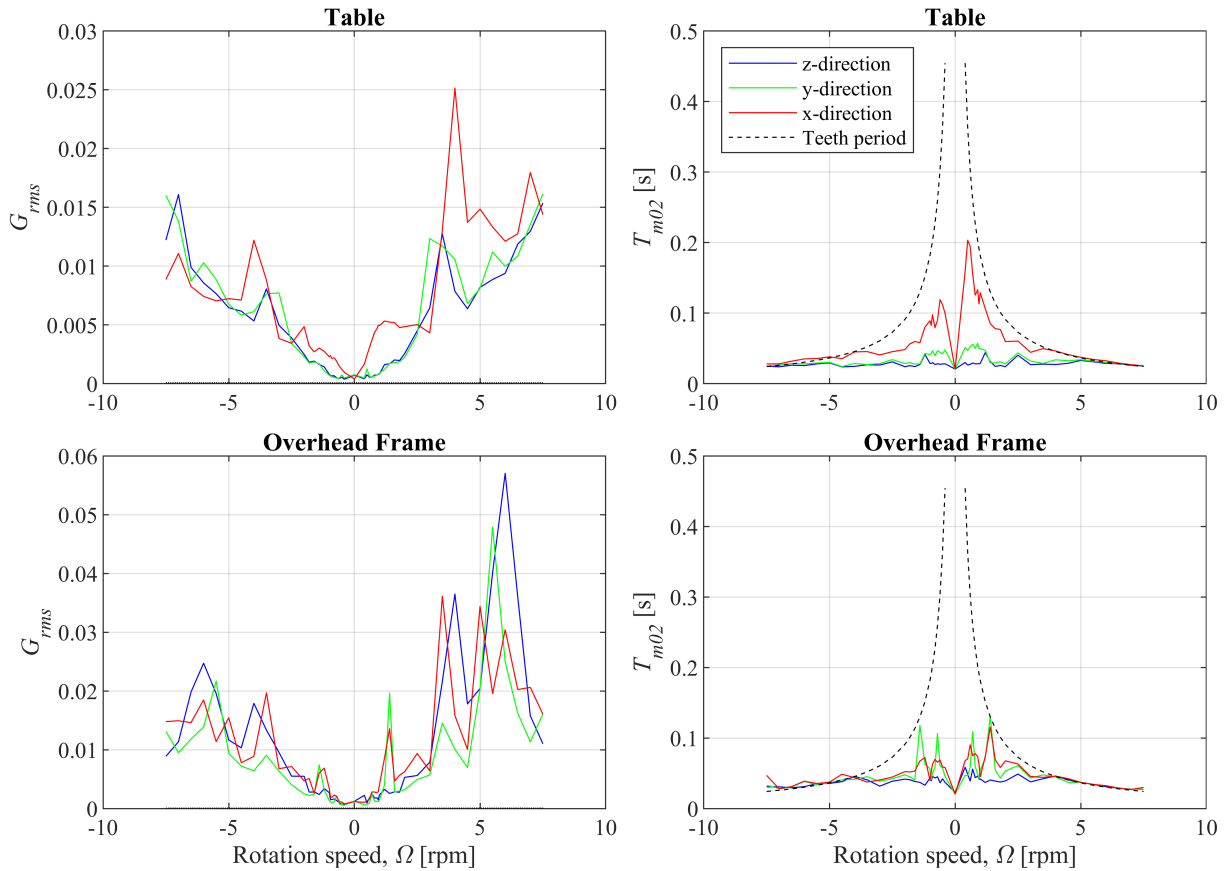


Figure 12: Root mean square G_{rms} (Left) and vibration period, T_{m02} (Right) in three directions on the table (upper panels) and on the overhead frame (lower panels) as a function of the rotation speed of the table. The horizontal dotted line near $G_{rms} = 0$ marks the intrinsic noise of the accelerometer sensor of 0.07 milli- G_{rms} (hardly distinguishable from the x-axis). The black dashed line marks the period of the teeth of the bearing-gear head assembly.

3.2 Performance of the pumping system

The performance of the pumping system is assessed by comparing the density profile created to the desired one. A small-scale version of the system described in Figure 8 is used for this test. The pumps, pipes and static mixer are the same as the ones used in the final system. Only the salt-water and fresh-water reservoirs are smaller, and the density profile is created in a smaller tank. For this test, the fresh-water density ρ_F and the salt-water density ρ_S are 998.9 kg/m³ and 1136.6 kg/m³, respectively. The system is tested for a linear density stratification, but can be equally used to generate any desired profile. To measure the density profile with sufficient accuracy and precision, the authors designed and developed a conductivity sensor (Figure 13a). This sensor is able to measure simultaneously conductivity and temperature within a 1 ml³ of fluid, up to a frequency of 1000 Hz, and with an accuracy of a hundredth of a millisiemens per centimetre (0.01 mS/cm) for the conductivity and a tenth of a degree Celcius (0.1°C) for the temperature. The sensor is calibrated using five solutions of known density and temperature (measured with a DMA 35 Basic density meter from Anton Paar). The range of densities used for the stratification ensures a linear relationship between the conductivity and density for a given temperature. The calibration procedure therefore allows the output voltage to be converted to density, correcting for temperature variations.

The conductivity probe is attached to a computer-controlled mechanical arm, allowing the stratification profile to be measured at a fixed speed. Figure 13b shows the results of the small-scale density stratification test, where a 13 cm tall linear profile was generated. The linear profile obtained with the pumping system is very close to the desired one, except in the bottom part of the profile where density is larger than the desired one. This is likely due to the very small flow rates required to create this small-scale stratification, which pushes the pumps to their limit in terms

of flow rate accuracy over small time scales. Another possible explanation is that, at pump start-up, the salt water may have been introduced slightly before the fresh water, thereby increasing the density of the initial (bottom) layer.

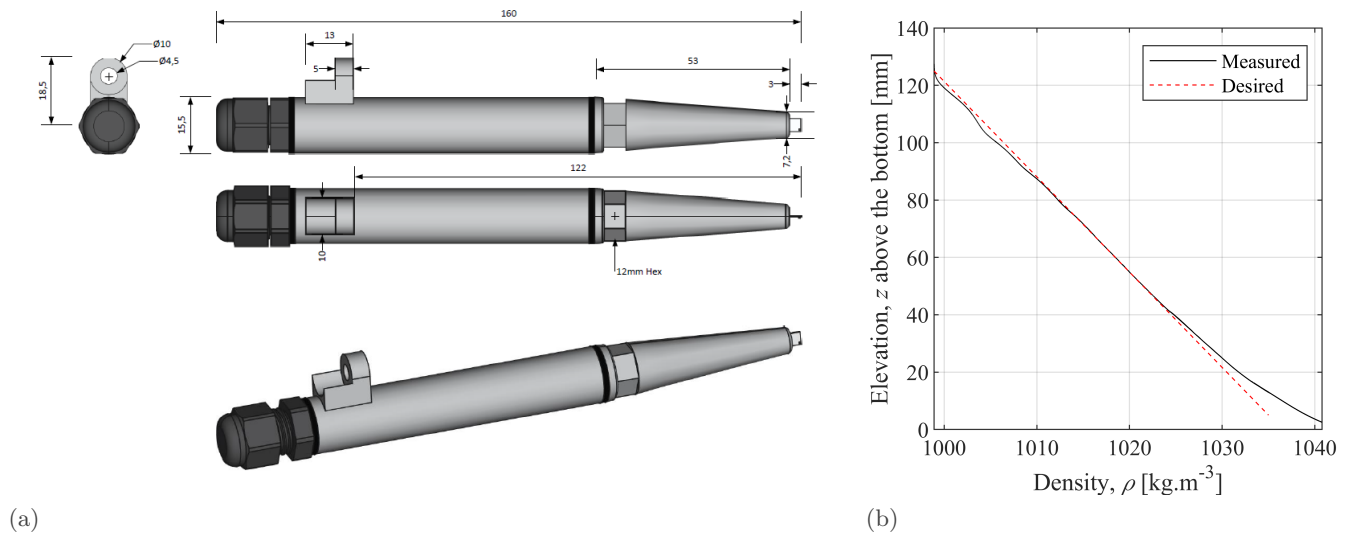


Figure 13: a) Design drawing of the conductivity and temperature measurement probe developed by the authors (mm). b) Desired and measured small-scale linear density stratification profile, created with the pumping system.

3.3 Performance of the 3D PTV system

To be able to measure the wave-induced current profile in both Lagrangian and Eulerian frameworks, it is crucial to track many particles within the whole volume, and to have relatively long tracks over several wave periods. Therefore, the performance of the 3D PTV system is determined by its ability to track numerous particles over multiple wave periods, with a high spatial coverage. Note that while the general performance of the LaVision MiniShaker has been evaluated in adjacent scientific fields (Schroder and Schanz, 2023), it is the first time that this system is used to study wave-induced currents.

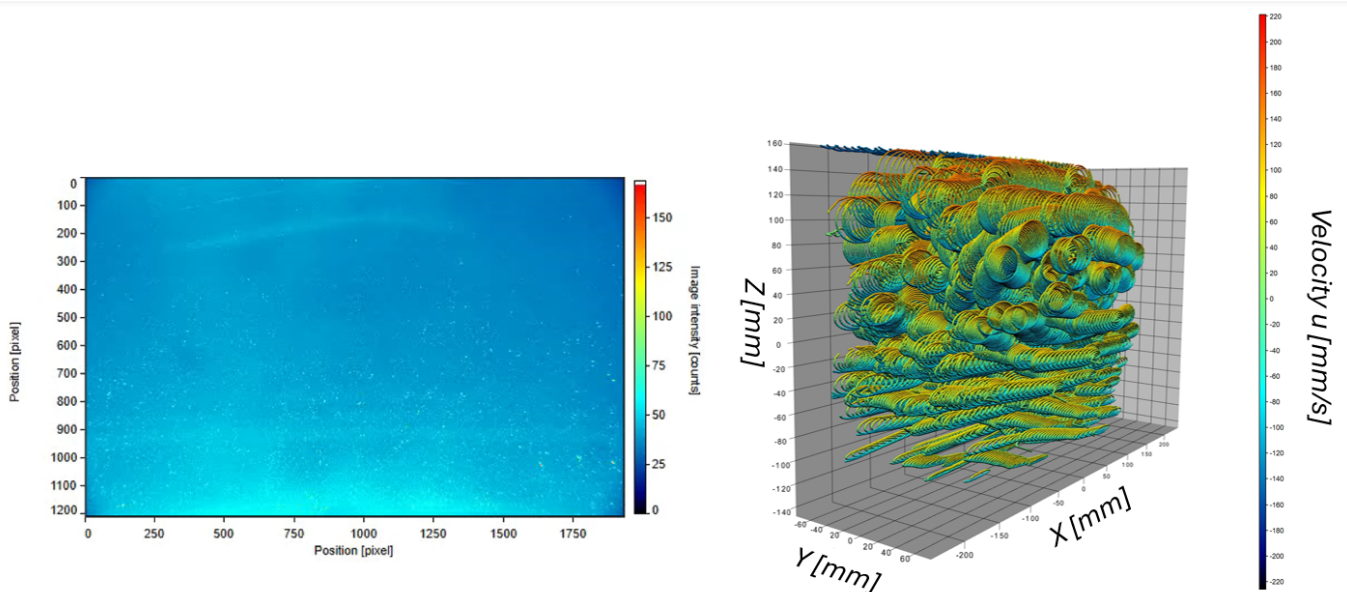


Figure 14: Results from the PTV system: the left panel shows a raw image recorded by one camera, in pixel space. The colour represents the intensity of each pixel, used in the post-processing. The right panel shows the complete track of 2354 particles tracked over 72 s in 3D: the x -axis is the cross-shore distance, y -axis is the depth-of-field (*i.e.*, the cross-flume distance), and z -axis is the vertical distance, all relative to the centre of the measured volume, in millimetres. The colour scale displays the horizontal velocity u , ranging from -220 to +220 mm/s.

The 3D PTV system was tested in a (non-rotating) wave flume in the Hydraulic Engineering Laboratory at TU Delft (set-up shown in Figure 10). Figure 14 displays a raw image recorded by one camera as part of a 72-s record. After post-processing the data using the ‘Shake-The-Box’ software, thousands of particles were tracked in time, in a 45-cm long (x -direction), 30-cm high (z -direction) and 15 cm deep (y -direction) volume. Figure 14 displays the complete tracks of the 2354 particles detected and tracked in three dimensions. Among those, 169 full tracks (*i.e.*, particles tracked from the beginning to the end of the video) were recorded in the whole volume, although these tracks are slightly more concentrated in the middle of the volume.

4 Guidance for DTP-Lab users: surface gravity waves under rotation

The first application of the turntable will be in combination with the rotating flume as shown in Figure 5b. This set-up will be used to investigate the effects of the Coriolis force on the currents generated by surface gravity waves, while keeping the wave field unaffected by Coriolis. Since surface gravity waves under rotation have never been studied in the laboratory before, further information is supplied here on the scaling associated with the generation of wave under rotation and laboratory effects. The aim of this section is to enable future users of the DTP-Lab, wishing to study aspects of surface waves under rotation, to determine which part of the real-world parameter space can be studied in the DTP-Lab (Section 4.1) and what experimental challenges may arise (Section 4.2).

4.1 Parameter space

Table 1 provides the range of wave and rotation parameters that occur in the field and those that can be realised in the DTP-Lab. Four primary parameters, the wave period T , the wave amplitude a , the water depth h and the Coriolis parameter $f = 2\Omega \sin(\theta)$ with Ω the rotation rate and θ the latitude, are used to calculate secondary dimensional and dimensionless parameters. The minimum, maximum and representative values of each of the primary parameters are given for the field and the DTP-Lab. All wave amplitudes are chosen to correspond to a constant wave steepness of 0.08, while the whole range of possible wave steepness ka is still given. The Coriolis parameter is zero at the equator and maximum at the poles.

Table 1: Parameter range in the field and in the DTP-Lab: The minimum and maximum values of the first 4 parameters are combined to calculate the min and max of the parameters below. The ‘representative’ values are used independently to calculate the parameters. The concept of the turntable is to be able to vary the Coriolis parameter, so the representative value of f , L_{R_w} , L_{R_c} , Ek^{-1} , Ro and f/ω are marked as ‘**Var**’, and this will be further explored in Figure 15 and 16. Note that the velocity $a\omega$ used to compute Re and Ro is the deep-water wave orbital velocity.

Parameters [unit]	Field [min - max - representative]	Laboratory [min - max - representative]
Wave period, T [s]	[2.00 - 18.00 - 8.00]	[0.50 - 2.00 - 0.7]
Wave amplitude, a [m]	[0.08 - 6.00 - 1.20]	[0.005 - 0.040 - 0.010]
Water depth, h [m]	[10 - 3000 - 30]	[0.15 - 0.40 - 0.20]
Coriolis parameter, f [s^{-1}]	[0.00 - 1.46×10^{-4} - 0.75×10^{-4}]	[0.00 - 1.57 - Var]
Wavelength, λ [m]	[6 - 500 - 96]	[0.4 - 2.7 - 0.7]
Phase velocity, c_p [m/s]	[3.12 - 28.10 - 12.00]	[0.77 - 1.84 - 1.03]
Stokes drift, U_s [m/s]	[0.02 - 0.15 - 0.08]	[0.005 - 0.016 - 0.008]
Wave Rossby radius, L_{R_w} [m]	[1.6×10^4 - ∞ - 1.2×10^5]	[0.49 - ∞ - Var]
Current Rossby radius, L_{R_c} [m]	[102 - ∞ - 782]	[0.003 - ∞ - Var]
Relative depth, kh	[0.31 - 37.00 - 1.96]	[0.390 - 6.40 - 1.75]
Wave steepness, ka	[0.01 - 0.35 - 0.08]	[0.01 - 0.35 - 0.08]
Wave Reynolds number, Re	[1.8×10^4 - 1.1×10^7 - 1×10^6]	[275 - 4410 - 787]
(inverse) Wave Ekman number, Ek^{-1}	[0 - 140 - 10]	[0 - 6.0×10^4 - Var]
Rossby number, Ro	[21 - ∞ - 100]	[0.02 - ∞ - Var]
f/ω	[0 - 5.6×10^{-4} - 1.3×10^{-4}]	[0 - 0.5 - Var]

These primary parameters are then used to calculate several dimensional parameters shown in Table 1: the wavelength λ , the phase speed c_p , the Stokes drift at the surface $U_s = \frac{g(ka)^2 \cosh(2kh)}{\omega \sinh(2kh)}$ with $\omega = 2\pi/T$ the angular frequency, the wave Rossby radius ($L_{R_w} = c_p/f$) and the current Rossby radius ($L_{R_c} = U_s/f$). The Rossby radii indicate either the length of the wave (current) or the distance the wave (current) needs to travel before being significantly affected by the rotation.

The primary parameters are also used to calculate several non-dimensional parameters shown in Table 1: the relative water depth kh , the waves steepness ka , the wave Reynolds number ($Re = a^2\omega/\nu$), which represents the ratio of inertial forces to viscous forces, the Rossby number ($Ro = a\omega/(\lambda f)$), which represents the ratio of inertial forces to the Coriolis force, the ratio f/ω , and the (inverse) wave Ekman number ($Ek^{-1} = f/(\nu 8k^2)$). The latter is the inverse of an Ekman number with the characteristic length scale set to the Stokes depth; it determines the relative importance of rotation and viscosity. Note that the (eddy) viscosity ν used to compute the parameters is of the order of $10^{-3} \text{ m}^2/\text{s}$ in the field (Cunningham et al., 2022), but we set it to be equal to the kinematic viscosity in the lab ($10^{-6} \text{ m}^2/\text{s}$).

While the wave steepness and water depth regimes are the same in the lab and the field, the Stokes drift is one order of magnitude lower in the lab. The wave Reynolds numbers reached in the lab are much smaller than in the field, although the turbulent regime is still achievable in the lab. The range of rotation of the turntable is 4 orders of magnitude larger than the f experienced on Earth (note that θ in the lab is 90 degrees, corresponding to the pole in the field). As a consequence, the (inverse) wave Ekman number lies between 0 and 140 in the field (Huang, 1979) but can be much larger in the lab. In addition, the ratio $f/\omega < 1$ for both the lab and field, but it is mainly 2 to 4 orders of magnitude larger in the lab than in the field, since the order of magnitude matches only for a turntable rotation of 0.01 rpm. This is also the case for the Rossby number which is 2 orders of magnitude lower in the lab than in the field, and match the field with a value of 78 only for a turntable rotation of 0.01 rpm.

The variation of the (inverse) wave Ekman number, Rossby number and f/ω parameter as a function of the turntable's angular velocity is shown in Figure 15. It is clear that the range of value for the field (grey area) for these parameters are only reached in the lab for very slow rotation speeds (log scale used in Figure 15). In the context of surface wave under rotation, the rotational force is, for most rotation speed, relatively stronger in the lab than in the field.

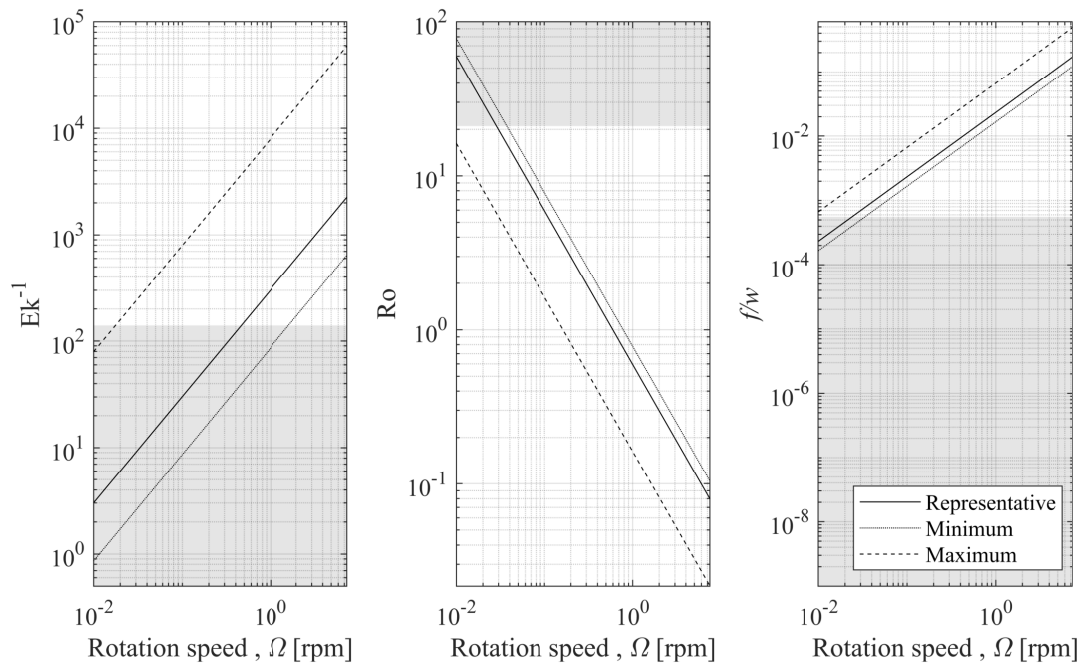


Figure 15: (Inverse) wave Ekman number (*left*), Rossby number (*middle*) and f/ω parameter (*right*) as a function of the turntable's angular velocity. These dimensionless parameters are computed using the minimum (min), maximum (max) and representative value of the primary parameters presented in Table 1. The grey area marks the range of values for the field.

While the turntable's purpose is to artificially increase the rotational force to study the effect of Coriolis, it is still important to assess whether rotation is expected to affect the wave field and/or current field. For the wave field, the wave Rossby radius L_{R_w} is used for this purpose (Table 1). The Rossby radius is the length scale at which rotational effects become as important as gravity wave effects. For a given wave (hence phase velocity, $c_p = \omega/k$) and Coriolis parameter f , if the wavelength (λ) is longer than the *wave Rossby radius*, or if the wave propagates over a distance longer than the *wave Rossby radius*, then the wave will feel the effect of rotation. For the wave-induced current field, the same concept applies with the *current Rossby radius*, which is calculated using the Stokes drift at the surface. Figure 16 shows the ratio of the wavelength over the *wave Rossby radius*, λ/L_{R_w} (left panel), the effective flume

length Δx over the *wave Rossby radius*, $\Delta x/L_{R_w}$ (middle panel) and the effective flume length over the *current Rossby radius*, $\Delta x/L_{R_c}$ (right panel) for a representative depth and wave steepness. Note that $\lambda/L_{R_w} = f/T$ is independent from h and a . For the wave field not to be (significantly) affected by rotation, both λ/L_{R_w} and $\Delta x/L_{R_w}$ should be (much) lower than 1. For the current field to be affected by rotation, $\Delta x/L_{R_c}$ should be larger than 1. Depending on the experiment objectives, one may want to fall inside or outside the grey areas, and can find the suitable range of frequency and rotation by combining the subplots.

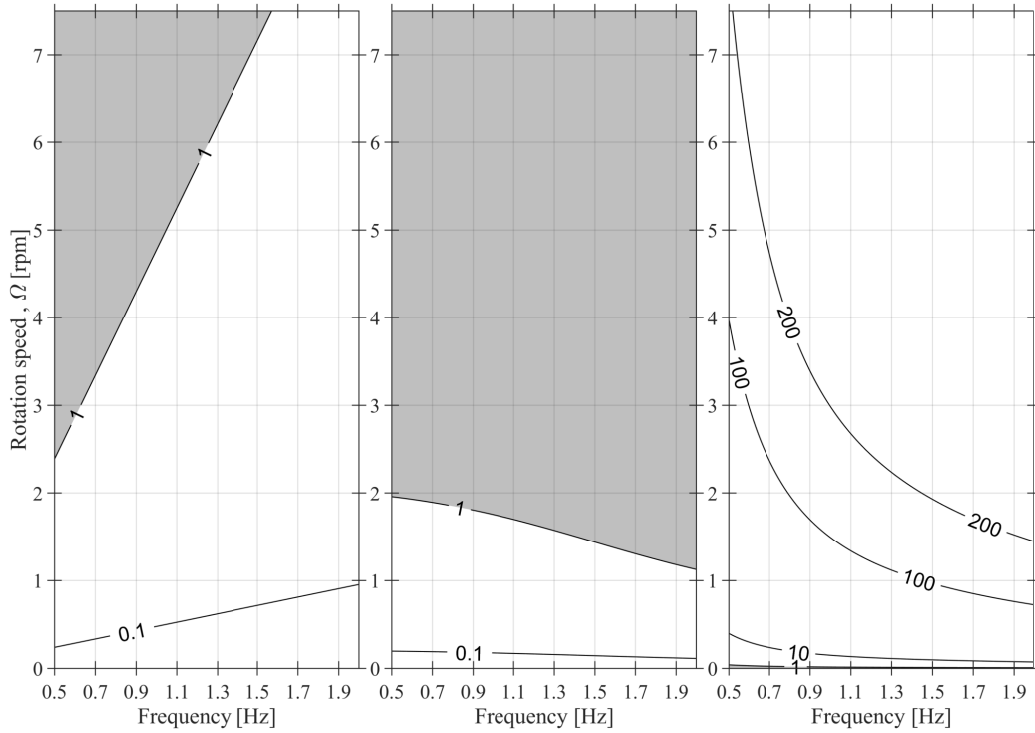


Figure 16: Contour plot of λ/L_{R_w} (left), $\Delta x/L_{R_w}$ (middle) and $\Delta x/L_{R_c}$ (right) as a function of the turntable's angular velocity and wave frequency, for a representative depth $h = 0.20$ m and $ka = 0.08$. Here, λ is the wavelength, Δx the effective flume length (3.30 m), L_{R_w} and L_{R_c} are, respectively, the wave and current Rossby radii (Table 1). The grey shaded areas correspond to $\lambda/L_{R_w} > 1$, $\Delta x/L_{R_w} > 1$ and $\Delta x/L_{R_c} < 1$, respectively.

The influence of rotation on the wave field is expected to deflect wave propagation and alter its direction, which is expected to result in a complex three-dimensional wave pattern. Experiments aiming to investigate such wave fields should employ a method capable of capturing the free surface in three dimensions, such as the Schlieren method.

4.2 Laboratory effects

First, the effect of the turntable's rotation on the water surface is investigated. The centrifugal effect of rotation causes a deformation of the free surface, which takes the shape of a parabola with the lowest point located at the centre of rotation. The general formulation for the water depth, $h(r)$ at constant pressure in a cylinder is given by (Dumitru et al., 2024):

$$h(r) = \frac{\Omega^2 r^2}{2g} + h_0, \quad (3)$$

where $\Omega = 2\pi[rpm]/60$ is the rotation of the table in radians per second, r is the radius, g is the acceleration due to gravity, and h_0 is the water depth at the centre of rotation. The aspect ratio of the rotating flume being 10 ($L/W=5/0.5=10$, with L and W respectively the length and width of the flume), it is assumed that the deformation is mainly 2-dimensional hence can be represented by the centre line along the flume. The free surface elevation relative to the non-rotating still water level, along the length of such a 'long' rotating flume (rectangular tank) is given by (Monteiro et al., 2020):

$$\Delta h = \frac{\Omega^2(x^2)}{2g} - \frac{\Omega^2(L^2)}{24g}, \quad (4)$$

with x the along-flume coordinate in metres (with the origin in the centre of rotation).

Figure 17 shows the water level difference between the free surface under rotation and the still water level prior to rotation, for both the centre of the flume (centre of rotation) and the paddle at its rest position. To keep the water level at the wavemaker constant for all experiments under rotation, the non-rotating water depth should be adjusted accordingly. Users should be aware that water level differences along the flume may influence wave propagation – the greater the difference, the more significant the potential effect – but further research is needed to fully understand these interactions.

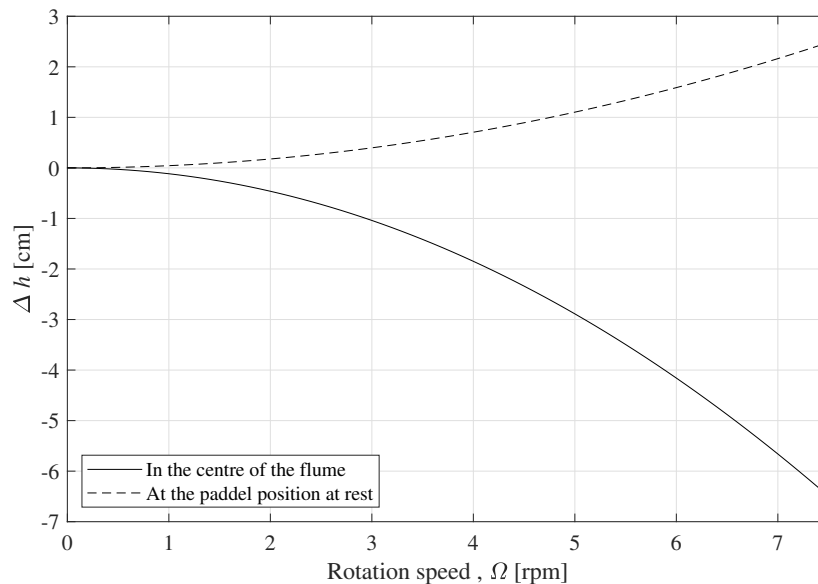


Figure 17: Water level difference, Δh between the free surface under rotation and the still water level prior to rotation, for both the centre of the flume (centre of rotation) and the paddle at its rest position.

Secondly, under rotation, the time scale associated with adjustment of the fluid to the final state of rigid-body rotation is the Ekman timescale $t_E = h/\sqrt{\nu\Omega}$ (Greenspan and Howard, 1963; Vallis, 2017), where h is the water depth in metre and ν the kinematic viscosity ($10^{-6} \text{ m}^2/\text{s}$). We suggest to wait at least $2 t_E$ before starting wave generation (see Figure 18).

Finally, the effect of the turntable's rotation (Section 3.1) on the water surface that is undisturbed by waves generated by the wave generator is investigated. Multiple resistive wave gauges were installed in the flume, including one at the centre (along the axis of rotation) and one at 1.65 m from the centre. Each wave gauge records the free surface at 125 Hz, with an accuracy of $\pm 0.1 \text{ mm}$. The variance density spectrum of the free surface time series (about 180 seconds long) is obtained with a Fourier transform, using Hamming-window of 40 s with 50 % overlap. The spectral wave amplitude based on the zeroth-order moment of the spectrum (a_{rms}) and the spectral wave period based on the second-order moment (T_{m02}) is calculated for the analysis. Figure 18 shows these two parameters as a function of the rotation speed for the wave gauge located in the middle of the flume. For rotation speeds below $\pm 7.0 \text{ rpm}$, vibrations from the table only generate very small oscillations with amplitudes below $a_{rms} = 0.5 \text{ mm}$. These oscillations reach more than 1.2 mm for maximum rotation speed of $\pm 7.5 \text{ rpm}$. The peak in the spectral wave period does not correspond to the period of the teeth, as was the case for the table's vibration (Figure 12), but instead displays the same trend as the wave amplitude. Up to a rotation speed of $\pm 7.0 \text{ rpm}$, the wave period of the vibrations is lower than the waves periods generated by the wavemaker, and of much smaller amplitude. It is therefore suggested not to use a rotation speed larger than $\pm 7.0 \text{ rpm}$ for this type of application. This figure also confirms that negative rotation should be preferred over positive rotation for rotation speeds between 0.4-0.8 rpm.

Figure 18 also shows the amplitude and period measured after different Ekman timescales, where 0 Ekman time corresponds to a measurement performed as soon as the desired rotation speed was reached. The time series of surface elevation measurement started as soon as the subsequent Ekman time was reached. For both the amplitude and period, all symbols but the circle gather around the same value, meaning that the signal becomes stable after 1 Ekman timescale (so between 1 and 2 Ekman time scales).

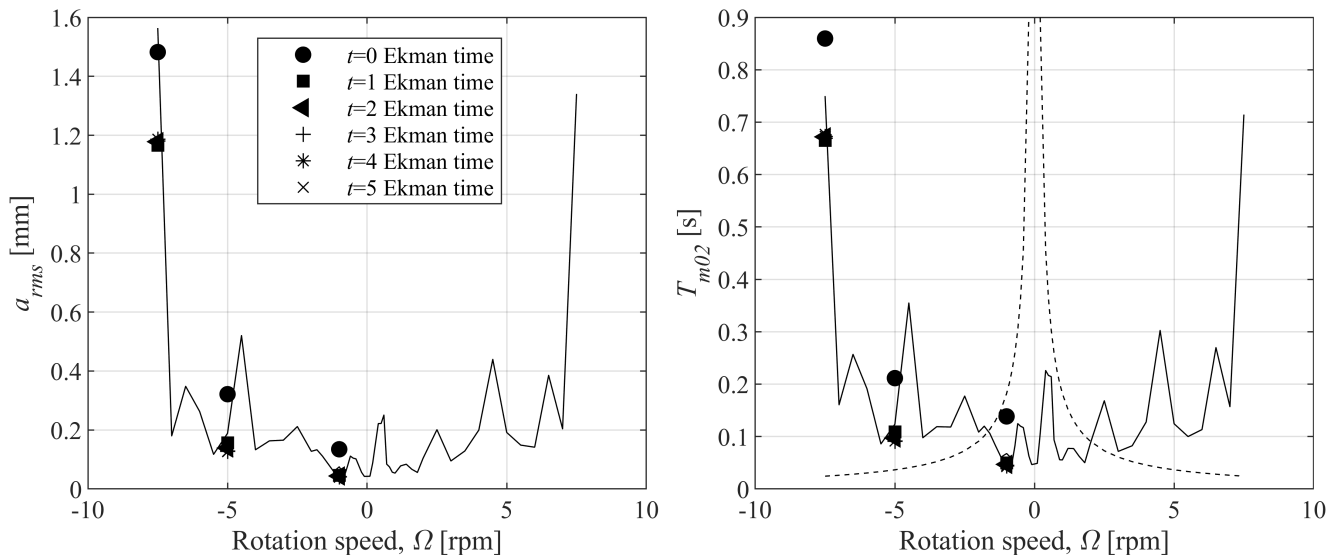


Figure 18: Wave amplitude, a_{rms} (Left) and wave period, T_{m02} (Right) obtained from free surface elevation measurements recorded at the centre of the flume as a function of the rotation speed. The black dashed line marks the period of the bearing-gear head assembly. The marker shows the values recorded at 0-5 Ekman time after initiation of rotation, for rotation speeds of 1, 5 and 7.5 rpm.

To investigate the effect of the turntable's precession due to deviation of the axis of rotation by 0.003 degrees from the vertical, the wave gauge at 1.65 m from the centre is used. Figure 19 shows the time series of free surface elevation for 1.0 and 5.0 rpm. The period of oscillation is the same as that of the table's rotation shown by the arrow (60 s and 12 s for 1.0 and 5.0 rpm, respectively). The amplitude of approximately 0.1 mm also corresponds to the expected amplitude at 1.65 m from the centre of rotation, given the 0.003-degree deviation in angle. This effect remains relatively small compared to the generated waves, but must be kept in mind when performing this type of experiment.

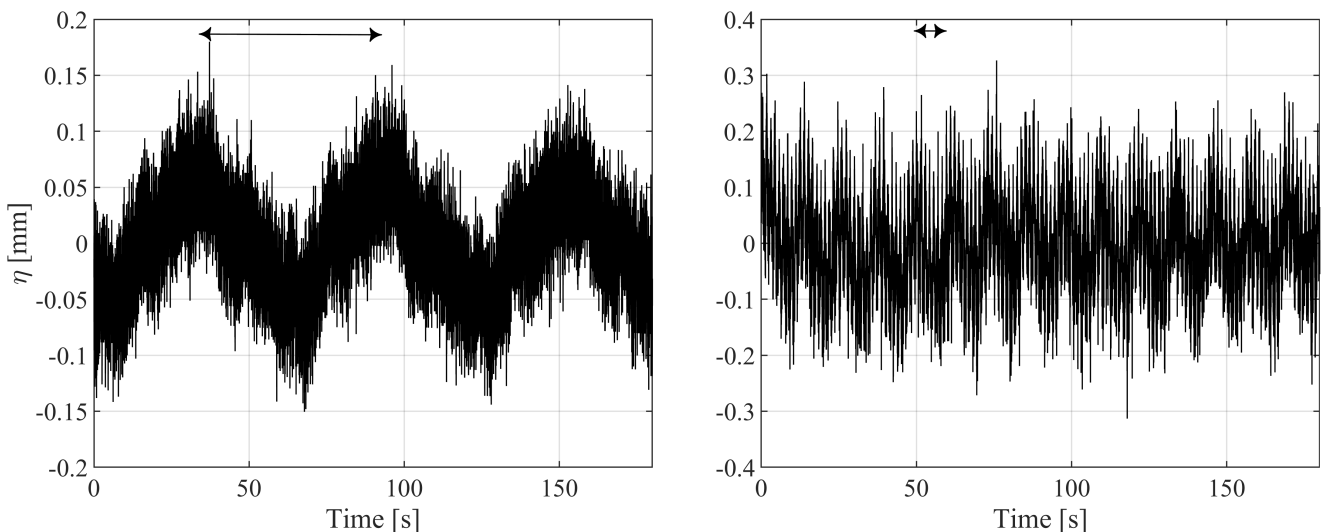


Figure 19: Time series of free surface elevation for 1.0 (Left) and 5.0 (Right) rpm, measured by the wave gauge located 1.65 m from the centre. The arrow marks the table's rotation period.

5 Conclusions

The Delta Transport Processes Laboratory was designed and constructed with the vision to provide a multi-purpose and multi-user lab, with novel infrastructures and state-of-the-art technologies. As such, the DTP-Lab is composed of:

- A 4.40-m diameter turntable,
- A 5-m long transportable rotating flume with full optical access, that can be placed onto the turntable
- A 12.7-m long stainless steel flume with full optical access, and a lock release system
- A piston, wet-back, force-controlled, surface wave generator
- A pumping system to create any type of density stratification in any of the two flumes
- A dedicated 3D PTV system, able to track thousands of particle and compute both the Lagrangian and Eulerian velocity.

A novel prototype internal gravity wave generator able to generate any type of internal wave in any type of density stratification is proposed for future DTP-Lab development.

The DTP-Lab turntable is the second largest rotating platform in the world that can be used to study the effect of rotation on fluid flow, after the Coriolis platform at LEGI, Grenoble, France (Mercier et al., 2012). The TurLab rotating tank at the University of Turin, Italy (Suino et al., 2017) is of similar size but is restricted to experiments in a round basin, while the rotating basin at the University of Science and Technology in Trondheim, Norway was decommissioned a few years ago. The DTP-Lab will pioneer the study of free surface wave and wave-induced current under rotation. To the authors' knowledge, the effect of Coriolis forces on the currents induced by surface gravity waves has never been studied in laboratory experiments before. The combination of the turntable and rotating flume at this scale is unique in the world at the time of writing this technical note.

The stainless steel flume, if used for internal gravity waves in the future, will be one of the longest internal wave flume in the world. The still proposed internal gravity wave generator differs from the 'Magic Carpet' (Dobra et al., 2019) by the fact that it is positioned vertically (and not horizontally at the bottom), and could thus produce a broad range of velocity-depth structures (shapes) suitable for a broad range of density stratifications and wave types. It is however very similar to the ones used in ENS Lyon (Dossmann et al., 2017), albeit somewhat larger and taller and will be used in a much longer flume. Finally, the interchangeability of both wave generators, since the rotating flume and the stainless steel flume have the same width and depth, increases the scope of possible application of the DTP-Lab.

Performance test of the turntable, pumping system and PTV system designed by the authors demonstrated the accuracy and suitability of the new infrastructure to accommodate high-standard research. The DTP-Lab will accommodate the first and largest experiment on free surface waves under rotation, with a specific focus on the effect of the Coriolis forces on the wave-induced current. Beyond these objectives, the DTP-Lab was designed in an user-friendly and adaptable way, with a 'plug and play' 3D PTV system.

The performance tests of the turntable and rotating flume showed that the turntable should preferably be operated in the negative (anti-clockwise) direction, particularly at rotation speeds between 0.4–0.8 rpm. Rotation speeds above ± 7.0 rpm should be avoided, and speeds in the range of ± 3.3 – 3.7 are also discouraged due to the risk of increased vibrations.

Acknowledgements

The authors would like to thank the Hydraulic Engineering Laboratory staff who helped us along the process: Jennifer Rietdijk, Frank Kalkman, Arie van der Vlies and Arno Doorn. We would also like to thank Evert Verduin and Jeroen Koning from DEMO. We want to thank Daan ter Meulen and Alessandro Antonini for helping us with the accelerometers' deployment and measurements. Finally, we would like to thank Louis Gostiaux, Matthieu Mercier, Sylvain Joubaud, Samuel Viboud and Michael Hallhouse for sharing their scientific and technical knowledge during the design of the facility.

Funding

The DTP-Lab was funded by TU Delft strategic internal funds.

Author contributions (CrediT)

PB: Conceptualisation, Design, Data curation, Formal analysis, Methodology, Validation, Writing – original draft, Writing – review and editing. LM: Conceptualisation, Design, Writing – review and editing. CW: Conceptualisation, Design, Writing – review and editing. PvdG: Conceptualisation, Design, Technical support. DdG: Conceptualisation, Design, Formal analysis, Construction. JM: Conceptualisation, Design, Methodology. SvH: Conceptualisation, Design, Construction. LL: Conceptualisation, Design, Construction. JvM: Conceptualisation, Construction. MH: Conceptualisation, Construction. RMW: Construction. CW: Conceptualisation, Technical support. BH: Conceptualisation. TvdB: Funding acquisition, Conceptualisation, Design, Formal analysis, Methodology, Writing – original draft, Writing – review and editing.

Use of AI

No AI was used in the preparation of this work.

Data access statement

The data acquired in the study will be made available on reasonable request.

Conflict of interest (COI)

There is no conflict of interest.

References

- Allshouse, M. and Swinney, H. (2020). Dependence of internal wave bolus transport on pycnocline thickness. *Geophysical Research Letters*, **47**. DOI:10.1029/2020GL086952.
- Calvert, R., Whittaker, C., Raby, A., Taylor, P., Borthwick, A. and van den Bremer, T.S. (2019). Laboratory study of the wave-induced mean flow and set-down in unidirectional surface gravity wave packets on finite water depth. *Physical Review Fluids*, **4**(11), 114801.
- Chen, Z., Zhang, Q., Wu, Y. and Ji, C. (2022). A modified breaker index formula for depth-induced wave breaking in spectral wave models. *Ocean Engineering*, **264**.
- Cunningham, H., Higgins, C. and van den Bremer, T. (2022). The role of the unsteady surface wave-driven Ekman–Stokes flow in the accumulation of floating marine litter. *Journal of Geophysical Research: Oceans*, **127**. DOI: 10.1029/2021JC018106.
- Dobler, D., Huck, T., Maes, C., Grima, N., Blanke, B., Martinez, E. and Ardhuin, F. (2019). Large impact of Stokes drift on the fate of surface floating debris in the South Indian Basin. *Marine Pollution Bulletin*, **148**, 202–209. ISSN 0025326X. DOI:10.1016/j.marpolbul.2019.07.057.
- Dobra, T., Lawrie, A. and Dalziel, S. (2019). The magic carpet: an arbitrary spectrum wave maker for internal waves. *Experiments in Fluids*, **172**.
- Dossmann, Y., Pollet, F., Odier, P. and Dauxois, T. (2017). Mixing and formation of layers by internal wave forcing. *Journal of Geophysical Research: Oceans*, **122**(12), 9906–9917. DOI:https://doi.org/10.1002/2017JC013309.
- Dumitru, R., Chiriacescu, B., Sanda Chiriacescu, F., Barna, V., Miron, C. and Berlic, C. (2024). Simple experiment and simulation of a rotating liquid's free surface. *Romanian Reports in Physics*, **76**, 906.

- Fraser, C.I., Morrison, A.K., Hogg, A.M., Macaya, E.C., van Sebille, E., Ryan, P.G., Padovan, A., Jack, C., Valdivia, N. and Waters, J.M. (2018). Antarctica's ecological isolation will be broken by storm-driven dispersal and warming. *Nature Climate Change*, **8**(8), 704–708. ISSN 1758-678X, 1758-6798. DOI:10.1038/s41558-018-0209-7.
- Gostiaux, L., Didelle, H., Mercier, S. and dauxois, T. (2007). A novel internal waves generator. *Experiments in Fluid*, **42**, 123–130. DOI:10.1007/s00348-006-0225-7.
- Greenspan, H.P. and Howard, L.N. (1963). On a time-dependent motion of a rotating fluid. *Journal of Fluid Mechanics*, **17**(03), 385.
- Grue, J. and Kolaas, J. (2017). Experimental particle paths and drift velocity in steep waves at finite water depth. *Journal of Fluid Mechanics*, **810**, R1. DOI:10.1017/jfm.2016.726.
- Hansen, J. and Svendsen, I. (1984). A theoretical and experimental study of undertow. *Coastal Engineering Proceedings*, 2246–2262.
- Hasselmann, K. (1970). Wave-driven inertial oscillations. *Geophysical and Astrophysical Fluid Dynamics*, **1**, 463–502. DOI:10.1080/03091927009365783.
- Higgins, C., Vanneste, J. and van den Bremer, T.S. (2020). Unsteady Ekman-Stokes dynamics: Implications for surface wave-induced drift of floating marine litter. *Geophysical Research Letters*, **47**(18), e2020GL089189. DOI: <https://doi.org/10.1029/2020GL089189>.
- Hill, D. (2002). General density gradients in general domains: The 'two-tank' method revisited. *Experiments in Fluid*, **32**, 434–440.
- Horn, D., Imberger, G. and Ivey, G. (2001). The degeneration of large-scale interfacial gravity waves in lakes. *Journal of Fluid Mechanics*, **434**, 181–207.
- Huang, N.E. (1979). On surface drift currents in the ocean. *Journal of Fluid Mechanics*, **91**(1), 191–208.
- Hwung, H. and Lin, C. (1991). The mass transport of waves propagating on a sloping bottom. *Coastal Engineering Proceedings*, 544–556.
- Iwasaki, S., Isobe, A., Kako, S., Uchida, K. and Tokai, T. (2017). Fate of microplastics and mesoplastics carried by surface currents and wind waves: A numerical model approach in the sea of Japan. *Marine Pollution Bulletin*, **121**(1), 85–96. ISSN 0025-326X. DOI:<https://doi.org/10.1016/j.marpolbul.2017.05.057>.
- Lentz, S.J. and Fewings, M.R. (2012). The wind- and wave-driven inner-shelf circulation. *Annu. Rev. Mar. Sci.*, **4**, 317–343.
- Longuet-Higgins, M.S. and Stewart, R.W. (1962). Radiation stress and mass transport in gravity waves, with application to 'surf beats'. *Journal of Fluid Mechanics*, **13**(4), 481–504.
- Matsunaga, N., Takehara, K. and Awaya, Y. (1994). The offshore vortex train. *Journal of Fluid Mechanics*, **276**, 113–124.
- Mercier, M., Mathur, M., Gostiaux, L., Gerkema, T., Magalhaes, J., Da Silva, J. and Dauxois, T. (2012). Soliton generation by internal tidal beams impinging on a pycnocline: laboratory experiments. *Journal of Fluid Mechanics*, **704**, 37–60. DOI:10.1017/jfm.2012.191.
- Miche, R. (1944). Mouvements ondulatoires des mers en profondeur constante ou décroissante. *Ann. des Ponts et Chaussées Ch.* **144**, 131–406.
- Monteiro, M., Tornaria, F. and C., M.A. (2020). Experimental analysis of the free surface of a liquid in a rotating frame. *European Journal of Physics*, **41**.
- Moulton, M., Suanda, S., Garwood, J., Kumar, N., Fewings, M. and Pringle, J. (2022). Exchange of plankton, pollutants, and particles across the nearshore region. *Annual Review of Marine Science*, **15**, 167–202. DOI:<https://doi.org/10.1146/annurev-marine-032122-115057>.
- Onink, V., Wichmann, D., Delandmeter, P. and van Sebille, E. (2019). The role of Ekman currents, geostrophy, and Stokes drift in the accumulation of floating microplastic. *Journal of Geophysical Research: Oceans*, **124**(3), 1474–1490. DOI:<https://doi.org/10.1029/2018JC014547>.

- Paprota, M., Sulisz, W. and Reda, A. (2016). Experimental study of wave-induced mass transport. *Journal of Hydraulic Research*, **54**(4), 423–434. DOI:10.1080/00221686.2016.1168490.
- Pearson, B. (2018). Turbulence-induced anti-Stokes flow and the resulting limitations of large-eddy simulation. *Journal of Physical Oceanography*, **48**(1), 17–122.
- Pezerat, M., Bertin, X., Martins, K. and Lavaud, L. (2022). Cross-shore distribution of the wave-induced circulation over a dissipative beach under storm wave conditions. *Journal of Geophysical Research: Oceans*, **127**.
- Schanz, D., Gesemann, S. and Schroder, A. (2016). Shake-the-box: Lagrangian particle tracking at high particle image densities. *Experiments in Fluids*, **57**.
- Schroder, A. and Schanz, D. (2023). 3D Lagrangian particle tracking in fluid mechanics. *Annual Review of Fluid Mechanics*.
- Sciacchitano, A., Leclaire, B. and Schrider, A. (2021). Main results of the first data assimilation challenge. *14th International Symposium on Particle Image Velocimetry – ISPIV2021*.
- Sellappan, P., Alvi, F.S. and Cattafesta, L.N. (2020). Lagrangian and Eulerian measurements in high-speed jets using multi-pulse shake-the-box and fine scale reconstruction. *Experiments in Fluids*, **61**.
- Stokes, G. (1847). On the theory of oscillatory waves. *Transactions of the Cambridge Philosophical Society*, **8**, 441–445.
- Suino, G., Miyamoto, H., Bertaina, M., Casu, R., Cotto, G., Forza, R., Manfrin, M., Mignone, M., Mulas, R., Onorato, M., Youssef, A., Caruso, R., Contino, G., Guardone, N., Bacholle, S., Gorodetzky, P., Jung, A., Parizot, E., Prevôt, G., Barrillon, P., Dagoret-Campagne, S., Blin, S. and Rabanal, J. (2017). The EUSO@Turlab project: Results from phase ii. *35th International Cosmic Ray Conference (ICRC2017)*, **301**. DOI:10.22323/1.301.0422.
- Sutherland, B.R., DiBenedetto, M., Kaminski, A. and van den Bremer, T. (2023). Fluid dynamics challenges in predicting plastic pollution transport in the ocean: A perspective. *Phys. Rev. Fluids*, **8**, 070701. DOI:10.1103/PhysRevFluids.8.070701.
- Ursell, F. (1950). On the theoretical form of ocean swell on a rotating earth. *Geophysical Journal International*, **6**(s1), 1–8. DOI:https://doi.org/10.1111/j.1365-246X.1950.tb02968.x.
- Vallis, G.K. (2017). *Atmospheric and Oceanic Fluid Dynamics: Fundamentals and Large-Scale Circulation*, Cambridge University Press, 2 edition.
- van den Bremer, T., Yassin, H. and Sutherland, B. (2019a). Lagrangian transport by vertically confined internal gravity wavepackets. *Journal of Fluid Mechanics*, **864**, 348–380. DOI:10.1017/jfm.2019.30.
- van den Bremer, T.S. and Breivik, Ø. (2017). Stokes drift. *Phil. Trans. R. Soc. Lond. A*, **376**, 20170104.
- van den Bremer, T.S., Whittaker, C., Calvert, R., Raby, A. and Taylor, P.H. (2019b). Experimental study of particle trajectories below deep-water surface gravity wave groups. *Journal of Fluid Mechanics*, **879**, 168–186. DOI: 10.1017/jfm.2019.584.
- van Sebille, E., Aliani, S., Law, K.L., Maximenko, N., Alsina, J., A. Bagaev, M.B., Chapron, B., Chubarenko, I., Cózar, A., Delandmeter, P., Egger, M., Fox-Kemper, B., Garaba, S.P., Goddijn-Murphy, L., Hardesty, D., Hoffman, M., Isobe, A., Jongedijk, C., Kaandorp, M., Khatmullina, L., Koelmans, A.A., Kukulka, T., Laufkötter, C., Lebreton, L., Lobelle, D., Maes, C., Martinez-Vicente, V., Maqueda, M.A.M., Poulain-Zarcos, M., Rodriguez, E., Ryan, P.G., Shanks, A., Shim, W.J., Suaria, G., M. Thiel, T.S.v.d.B. and Wichmann, D. (2020). The physical oceanography of the transport of floating marine debris. *Environ. Res. Lett.*, **15**(2), 023003.
- Weber, J.E.H., Whitchelo, Y., Pirolt, J.A., Christensen, K.H., Rabault, J. and Jensen, A. (2023). Observations of transient wave-induced mean drift profiles caused by virtual wave stresses in a two-layer system. *Journal of Fluid Mechanics*, **975**, A12. DOI:10.1017/jfm.2023.864.